






Article

Winding Tensor Approach for the Analytical Computation of the Inductance Matrix in Eccentric Induction Machines

Javier Martinez-Roman , Ruben Puche-Panadero , Angel Sapena-Bano ,
Manuel Pineda-Sanchez * , Juan Perez-Cruz and Martin Riera-Guasp 

Institute for Energy Engineering, Universitat Politècnica de València, Camino de Vera s/n, 46022 Valencia, Spain; jmroman@die.upv.es (J.M.-R.); rupucpa@die.upv.es (R.P.-P.); asapena@die.upv.es (A.S.-B.); juperez@die.upv.es (J.P.-C.); mriera@die.upv.es (M.R.-G.)

* Correspondence: mpineda@die.upv.es; Tel.: +34-96-387-7000

Received: 29 April 2020; Accepted: 25 May 2020; Published: 28 May 2020



Abstract: Induction machines (IMs) are critical components of many industrial processes, what justifies the use of condition-based maintenance (CBM) systems for detecting their faults at an early stage, in order to avoid costly breakdowns of production lines. The development of CBM systems for IMs relies on the use of fast models that can accurately simulate the machine in faulty conditions. In particular, IM models must be able to reproduce the characteristic harmonics that the IM faults impress in the spatial waves of the air gap magneto-motive force (MMF), due to the complex interactions between spatial and time harmonics. A common type of fault is the eccentricity of the rotor core, which provokes an unbalanced magnetic pull, and can lead to destructive rotor-stator rub. Models developed using the finite element method (FEM) can achieve the required accuracy, but their high computational costs hinder their use in online CBM systems. Analytical models are much faster, but they need an inductance matrix that takes into account the asymmetries generated by the eccentricity fault. Building the inductance matrix for eccentric IMs using traditional techniques, such as the winding function approach (WFA), is a highly complex task, because these functions depend on the combined effect of the winding layout and of the air gap asymmetry. In this paper, a novel method for the fast and simple computation of the inductance matrix for eccentric IMs is presented, which decouples the influence of the air gap asymmetry and of the winding configuration using two independent tensors. It is based on the construction of a primitive inductance tensor, which formulates the eccentricity fault using single conductors as the simplest reference frame; and a winding tensor that converts it into the inductance matrix of a particular machine, taking into account the configuration of the windings. The proposed approach applies routine procedures from tensor algebra for performing such transformation in a simple way. It is theoretically explained and experimentally validated with a commercial induction motor with a mixed eccentricity fault.

Keywords: induction machines; inductance tensor; winding tensor approach; fault diagnosis; mixed eccentricity; winding asymmetries; discrete Fourier transform

1. Introduction

Induction machine (IM) maintenance, integrated in condition-based maintenance (CBM) systems [1–5], is a field of growing industrial interest, due to its widespread use in production lines, electrical vehicles, wind generators, etc. The failure of an IM can cause huge losses, due to unexpected breakdowns of machines and supply systems. To be responsive, CBMs must be able to operate on-line, in a non-invasive way, so that any fault can be detected in an incipient state and

corrective measures can be deployed before the fault gets worse [6–11]. This requires fast and simple fault diagnostic techniques [12], that can be implemented in embedded field devices, such as digital signal-processors (DSPs) or field-programmable arrays (FPGAs). One of such diagnostic techniques relies on the design of sliding mode observers (SMO) for observing IM states obtained from the healthy and faulty model. In [13], an SMO that uses only input quantity information for on-line broken rotor bar detection is proposed, and in [14], a high-order SMO is designed for detecting inter-turn short circuit faults in IMs. Recent developments [15,16] in this field propose the use of a reduced-order SMO for fault estimation, which is able to simultaneously obtain the exact estimation of state, actuator faults, sensor faults, and extra disturbances. In [16], a novel approach is proposed without employing the equivalent output error injection technology, to overcome the problem of the traditional SMO in application to Markovian jump systems, and in [15], a new proposal is made for avoiding the sliding surface switching problem. Another diagnostic technique is to run an electromechanical model of the machine [17–20] and compare the simulation outputs (currents and voltages) with the quantities measured at the machine terminals. Divergences between the predicted and the measured values are an indicator of a possible fault, especially if these differences increase over time.

The IM models needed in the aforementioned diagnostic techniques can be built using the finite elements method (FEM) with a very high accuracy [21–23], but FEM demands huge computing resources, in terms of time and memory, which hinders its use in low-power embedded units. A faster and leaner alternative is to use analytical models [23,24] that can reproduce the characteristic harmonics induced in the current by a given fault. Another diagnostic area in which IM models are used is in the training of neural networks or expert systems for fault diagnosis [25–31], which need thousands of tests performed under different working conditions with controlled degrees of a machine fault. In this area, again, the speed of analytical models can give them a decisive advantage over FEM models.

Different IM analytical models for fault diagnosis have been proposed in the technical literature, based on the machine equations expressed in different coordinate systems, such as $d - q$, revolving fields, etc. These models rely on the calculation of the self and mutual inductances between all the machines phases, and their derivatives, as a function of the rotor position. This is a complex, non-linear function, which depends on the windings configurations, and on the rotor position. Besides, in case of a faulty machine, the air gap length or the configuration of the windings may become asymmetrical, making it difficult to use labour-saving procedures that are valid only for symmetrical conditions. In particular, the eccentricity fault [32,33] gives rise to a non-uniform air gap length, which becomes a function of the angular coordinate. Moreover, this function can be different for each rotor position [34]. To overcome this difficulty, the analytical methods for calculating the inductance matrix commonly apply the simplification of considering a sinusoidal distribution of the spatial waves in the air-gap, thus limiting the calculation of the inductances to its fundamental harmonic component. Nevertheless, complex interactions between spatial and time harmonics are present in a faulty machine, but are missing in models restricted to the fundamental component.

Several approaches have been used in the technical literature for obtaining the inductance matrix needed in analytical models. Its components can be determined by direct measurements, as in [35,36], or computed numerically. FEM models have been used for inductance computation in [23], and in [37] a FEM model is combined with a Preisach model for iron loss evaluation. An alternative is to use analytical methods for inductance computation. In [38] a review of the existing methods for the analytical computation of self and mutual inductances in a rotating electrical machine are described, and a new approach based on energy method is presented. A drawback of the analytical methods is that they do not take into account the saturation, the iron path, or the end leakage inductances. In [39] these factors have been simulated via modified air gap length functions.

Instead of a direct, analytical computation of the inductances of phases with a complex winding layout, a successful approach is to start with the inductances of elementary coils, and to combine them via connection matrices to obtain the phase inductances [40]. This approach has been followed also in the winding function approach (WFA) [39]. In [41] the WFA has been combined with a conformal

transformation in order to take into account air gap length variations due to the slots. A drawback of these methods is that they need complex winding functions, which depend on the relative position of the coils and the rotor position. Moreover, these functions depend on the combined effect of the winding layout and of the air gap asymmetry, which makes their computation a highly complex task.

In this work, this line of research is followed, with two fundamental novelties: replacing the coils by the conductor as the basic, most simple winding unit, and using routine tensor algebra for the analytical computation of the inductance matrix. This approach allows decoupling the combined effects of the air gap asymmetry and of the winding configuration in the calculation of the inductance matrix, greatly simplifying its analytical computation. The proposed method for calculating the inductance matrix is developed in two steps:

1. First, a primitive inductance tensor is calculated in a reference frame that consists of a thin cylindrical sheet of a high number of parallel bars, statically fixed to the air gap. This can be considered, as [42] states, as a canonical coordinate system, in which the components of the primitive inductance tensor are the same for every IM, except for a scaling factor.
2. The primitive inductance tensor is transformed into the final one via a winding tensor [40], which contains the current-sheet generated by each phase when fed by a unit current, using routine tensor algebra procedures.

The proposed approach neatly decouples the geometrical configuration of the machine air gap (which can be asymmetrical), represented in the primitive inductance tensor, and the configuration of the phase windings (which can be arbitrarily complex), represented in the winding tensor. Both tensors are defined analytically in an independent way, which simplifies their formulation. Their combined effect, obtained using routine tensor algebra operations, gives the final IM inductance matrix in a simple and fast way, which may be denoted as the winding tensor approach (WTA).

The structure of the paper is the following one. In Section 2, the analytical model of the IM used in this work, in a natural coordinate system, is presented. The analytical computation of the inductance matrix that appears in this model is developed in Section 3 for the case of a healthy and an eccentric IM, using tensor algebra. In Section 4 tensor algebra is applied again to take into account different phase connections, as those imposed by a squirrel cage rotor. An experimental validation of the proposed approach is carried out using a commercial IM motor with a provoked mixed eccentricity fault. This motor is first simulated in Section 5, and the results are compared with those obtained from the experimental tests in Section 6. Finally, Section 7 presents the conclusions of this work.

2. Analytical Model of the IM Using a Natural Coordinate System

Let's consider a generic IM with n_s stator phases and n_r rotor phases, with a total number of phases $n = n_s + n_r$. Among the multiple coordinate systems that can be used for obtaining an analytical model of the IM (dq , symmetrical components, revolving fields, etc.), a natural coordinate system has been chosen in this work: each stator phase ($s_1, s_2 \dots s_{n_s}$) has its own axis as a stationary coordinate axis, and each rotor phase ($r_1, r_2 \dots r_{n_r}$) has its own axis as a moving coordinate axis, attached to the phase conductors. All the n phase currents in this coordinate system are considered to be independent variables, thus defining an n -dimensional space. From the point of view of the IM simulation, this choice has the advantage of directly giving the phase currents, without needing any further transformation.

In the natural coordinate system, two equations are needed to model the IM operation [40,43]

$$\begin{aligned}
 & \bullet \text{ Equation of voltage:} & e &= \mathbf{R}\mathbf{i} + \mathbf{L}\frac{d\mathbf{i}}{dt} + \mathbf{i}\frac{d\mathbf{L}}{d\theta}\dot{\theta} \\
 & \bullet \text{ Equation of torque:} & T &= R_\theta\dot{\theta} + J\frac{d\dot{\theta}}{dt} - \frac{1}{2}\mathbf{i}^t\frac{d\mathbf{L}}{d\theta}\mathbf{i}
 \end{aligned} \tag{1}$$

where the subscript t stands for the transpose operator. The quantities that appear in (1) are the following ones:

- i is the current tensor. Its components are the instantaneous current in each winding $i = [i_1, i_2, \dots, i_n]^t$.
- e is the voltage tensor. Its components are the instantaneous terminal voltages applied to each winding $e = [e_1, e_2, \dots, e_n]^t$.
- R is the resistance tensor. Its components are the resistances of all windings. It is a symmetrical dyadic tensor, an square array of n^2 constant components.
- L is the inductance tensor. Its components are the self and mutual inductances of all windings along the electrical axes. It is a symmetrical dyadic tensor, an square array of n^2 elements. It can be expressed as the sum of two components, one with the inductances corresponding to the main flux linkages L_m , and other with the leakage inductances L_σ , as

$$L = L_m + L_\sigma \quad (2)$$

End turns, end rings, and slot leakage inductances, included in the L_σ matrix, need to be pre-calculated, as usual in the technical literature, where explicit expressions for these inductances can be found in [44–46]. This work deals only with the analytical computation of L_m in (2). Linear behavior of the iron material will be assumed, as in [47]. This limitation of the analytical model can be overcome using a modified air gap length function to take into the saturation, as in [39].

- The rest of the terms that appear in (1) are the instantaneously applied shaft torque T , the frictional resistance of the shaft R_θ , and the moment of inertia J .

The equation of voltage in (1) can be expressed in a more condensed form making use of the tensor of flux linkages of the IM phases, $\varphi = Li$. Besides, neglecting the frictional resistance of the shaft ($R_\theta = 0$) in the equation of torque in (1), the set of electro-mechanical equations of the IM, in the natural coordinate system, is given by

$$\begin{cases} e = Ri + \frac{d\varphi}{dt} \\ T = J \frac{d\dot{\theta}}{dt} - \frac{1}{2} i^t \frac{dL}{d\theta} i \end{cases} \quad (3)$$

An implementation of (3) in a Simulink model is shown in Figure 1. The mutual inductances between the stator and rotor phases in L_m (2) depend on the rotor position, and must be updated at each step of the simulation.

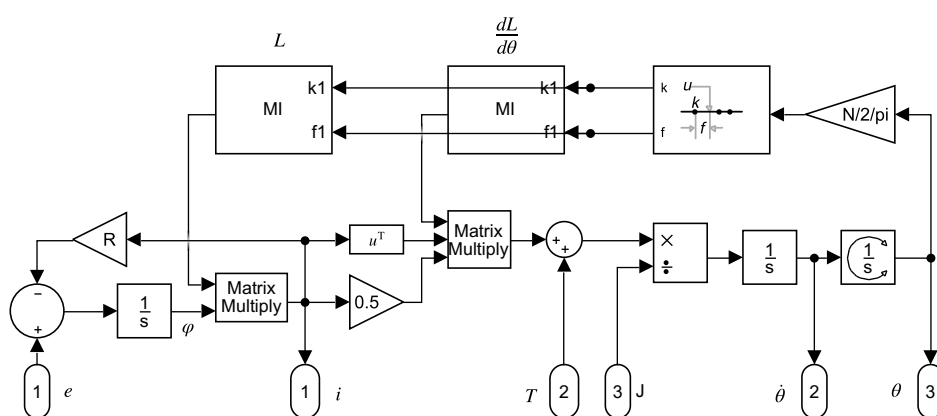


Figure 1. Analytical model that implements (3) in Simulink.

Transformation of the Coordinate System

The quantities i , e , R and L are tensors, that is, if a different coordinate system is chosen (for example, the hypothetical axis of symmetrical components, or a stationary dq coordinate system), these quantities remain invariant. Only their components (currents, voltages, self and mutual inductances, etc.) in the new coordinate system will be transformed, in the same way that an invariant vector

can have different components under different coordinate systems, in spite of not changing neither its modulus nor its orientation. In particular, if the current tensor is expressed in a coordinate system different than the natural one, its new components i' would be different than the old ones, i . Nevertheless, if the matrix C of the coordinate transformation is given, then the relation between the old components and the new ones can be expressed as

$$i = Ci' \quad (4)$$

and the transformation law of the rest of tensors e , R and L is given, applying tensor algebra, by

$$\begin{aligned} e' &= C^t e \\ L' &= C^t L C \\ R' &= C^t R C \end{aligned} \quad (5)$$

where C^t stands for the transpose of matrix C .

3. Computation of the Mutual Inductance Matrix Using Tensor Algebra

Neglecting the iron saturation and losses, mutual inductances depend only on the geometry of the system [48]. Therefore, their computation is done in this work in the spatial domain of the air gap, using the current-sheet generated by the phase currents i . The steps of this approach are:

1. Definition of the canonical coordinate system for representing the current-sheet distribution along the air gap periphery. In this system, the components of the tensors i and L_m are independent of the connections of the phase conductors.
2. Calculation of the current-sheet from the phase currents i . The winding tensor contains the connections between the conductors of the phases, which can be arbitrarily complex.
3. Definition of the primitive inductance tensor in the canonical coordinate system, which is independent of the layout of the winding, and the same for every IM, apart from a scaling factor.
4. Transformation of the inductance tensor to the natural coordinate system using tensor algebra (5).

3.1. The Components of the Current Tensor

The components of the current tensor are obtained first in the canonical coordinate system, where they are independent of the connections of the phase conductors, and after transformed to the natural coordinate system, using a winding tensor that represents the windings layout.

3.1.1. The Current Tensor in the Canonical Coordinate System

The physical representation of the current tensor i in rotating electrical machines is a current-sheet distributed along the air gap periphery [43]. The most suitable coordinate system to represent it consists in a thin cylindrical sheet of N parallel bars [40], statically placed at the air gap, as shown in Figure 2. The value of N must be high to achieve a high spatial resolution ($N = 3600$ in this work). The width of each individual bar is assumed to be $2\pi/N$, while its height is considered negligible. An electrical coordinate axis is attached to each conductor, thus defining a N dimensional space in which any current-sheet can be represented with up to $N/2$ spatial harmonics. This N dimensional space is spanned by a basis with N elements, given by

$$\begin{cases} u_{c1} &= [1, 0, 0, \dots, 0]^t \\ u_{c2} &= [0, 1, 0, \dots, 0]^t \\ &\dots \\ u_{cN} &= [0, 0, 0, \dots, 1]^t \end{cases} \quad (6)$$

where the k th basis element \mathbf{u}_{ck} has all components equal to 0 except the k th that is 1. The vectors \mathbf{u}_{ck} are unitary and orthogonal, and they form an ordered basis, which is called the standard or canonical basis. In this basis, the current-sheet can be represented as a linear combination of the basis elements as

$$\mathbf{i}_c = \sum_{k=1}^N i_{ck} \cdot \mathbf{u}_{ck} \quad (7)$$

where i_{ck} the current in conductor k . That is, the components of the current tensor in this coordinate system, \mathbf{i}_c , are simply the N currents through the N independent conductors

$$\mathbf{i}_c = [i_{c_1}, i_{c_2}, \dots, i_{c_N}]^t \quad (8)$$

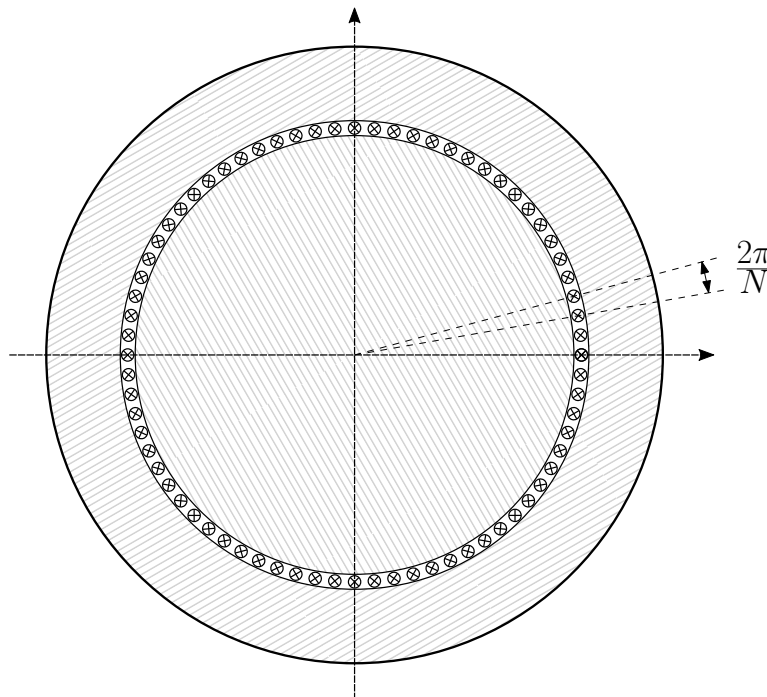


Figure 2. Coordinate system constituted by N independent conductors. A current-sheet with up to $N/2$ spatial harmonics can be represented in this system. The N components of the current tensor in this system, \mathbf{i}_c , are the currents through each conductor.

3.1.2. Transformation of the Current Tensor to Natural Coordinates

The current-sheet \mathbf{i}_c (8) can be also expressed in the natural coordinate system, using the n phase currents as independent variables. This n dimensional space is spanned by a basis formed by n basis vectors, n_s stator and n_r rotor vectors. In this basis, the current-sheet \mathbf{i}_c can be represented as a linear combination of the new basis vectors as

$$\mathbf{i}_c = \sum_{k=1}^n i_k \cdot \mathbf{z}_k \quad (9)$$

where i_k represents the current in phase k . Each basis vector in (9) has N components, which for the k th basis vector \mathbf{z}_k are the ampere-turns generated by phase k at each angular interval of Figure 2, when fed with a unit dc current. This value coincides with the number of conductors of phase k in each interval, with a \pm sign corresponding to the direction of the current.

$$\begin{cases} \mathbf{z}_1 = [z_{11}, z_{21}, z_{31}, \dots, z_{N1}]^t \\ \mathbf{z}_2 = [z_{12}, z_{22}, z_{32}, \dots, z_{N2}]^t \\ \vdots \\ \mathbf{z}_n = [z_{1n}, z_{2n}, z_{3n}, \dots, z_{Nn}]^t \end{cases} \quad (10)$$

The number of basis vectors in this new coordinate system (10) is much lower than in the primitive coordinate system (6). Nevertheless, they are neither unitary nor orthogonal.

The new vector basis (10) can be expressed in the canonical basis (6) as

$$\mathbf{z}_k = \sum_{l=1}^N z_{kl} \cdot \mathbf{u}_l \quad (11)$$

Using (10) and (11), (9) becomes

$$\mathbf{i}_c = \sum_{k=1}^n \sum_{l=1}^N i_k \cdot z_{kl} \cdot \mathbf{u}_l \quad (12)$$

This coordinate transformation can be formulated using a $(N \times n)$ transformation matrix \mathbf{C}_c as (4)

$$\mathbf{i}_c = \mathbf{C}_c \mathbf{i} \quad (13)$$

where the columns of \mathbf{C}_c are the new basis vectors (10),

$$\mathbf{C}_c = \begin{bmatrix} z_{11} & z_{12} & \cdots & z_{1n} \\ z_{21} & z_{22} & \cdots & z_{2n} \\ \vdots & \vdots & \ddots & \vdots \\ z_{N1} & z_{N2} & \cdots & z_{Nn} \end{bmatrix} \quad (14)$$

The transformation matrix \mathbf{C}_c represents the current constraints imposed by the connections between the conductors of each winding. Therefore, as Kron states in [40], this particular transformation matrix can be considered as one aspect of the transformation tensor \mathbf{C}_c , that will be referred to as the winding tensor. Its (i, j) element contains the number of phase conductors of phase j in an angular interval $\pi/2N$, centered at $i \cdot \frac{2\pi}{N}$. This winding tensor must be obtained for the N possible angular positions of the rotor ($\theta_k = k \cdot \frac{2\pi}{N}$, with $k = 0, \dots, N - 1$). Nevertheless, the columns of \mathbf{C}_c corresponding to the rotor phases for a given rotor position θ_k are the same as the columns defined with the rotor at the origin ($\theta_0 = 0$), but rotated k positions.

3.1.3. The Winding Tensor for Phases with the Same Configuration

In (14) no restrictions are imposed on the connections of the conductors of each phase, which can be arbitrarily complex, as in the case of asymmetrical windings (turn-to-turn short circuits, broken bars, etc.). Nevertheless, in case of a healthy machine, the configuration of all the phases of a particular winding (stator or rotor) is the same. Therefore, the vector column of \mathbf{C}_c corresponding to the k th stator phase is equal to the vector column of the first stator phase, but rotated $k \cdot N/n_s$ elements to the bottom. The same applies to the rotor phases, but in this case the rotation is $k \cdot N/n_r$ positions.

3.2. The Components of the Mutual Inductance Tensor

The components of the mutual inductance tensor will be obtained first in the canonical coordinate system, where they are independent of the connections of the phase conductors, and then transformed to the natural coordinate system, using the winding tensor.

3.2.1. The Primitive Inductance Tensor

In the canonical coordinate system (6), the mutual inductance tensor, L_{mc} , is a $N \times N$ square matrix

$$L_{mc} = \begin{bmatrix} L_{mc11} & L_{mc12} & \cdots & L_{mc1N} \\ L_{mc21} & L_{mc22} & \cdots & L_{mc2N} \\ \vdots & \vdots & \ddots & \vdots \\ L_{mcN1} & L_{mcN2} & \cdots & L_{mcNN} \end{bmatrix} \quad (15)$$

whose component (i, j) , L_{mcij} , is the mutual partial inductance [24] between the conductors placed at positions $i \cdot \frac{2\pi}{N}$ and $j \cdot \frac{2\pi}{N}$. The tensor L_{mc} (15) will be denoted as the primitive inductance tensor.

3.2.2. The Primitive Inductance Tensor of a Non-Eccentric IM

In case of IMs with uniform air gap, as represented in Figure 2, L_{mcij} depends only on the angular separation between conductors i and j , as given in [49]

$$L_{mc}(i, j) = L_{mcij} = \frac{\mu_0 \cdot l \cdot r \cdot \pi}{g} \cdot \left(\frac{1}{2} - \frac{|i - j|}{N} \right)^2 \quad (16)$$

where $\mu_0 = 4\pi \times 10^{-7} \text{ T}\cdot\text{m}\cdot\text{A}^{-1}$, l is the effective length of the stator bore, r is the radius at the center of the air gap, and g is the air gap length.

From (16), the components of L_{mc} are the same for every IM, except for the scaling factor $\frac{\mu_0 \cdot l \cdot r \cdot \pi}{g}$, which depends only on the geometrical dimensions of the machine, l , r and g . Besides, L_{mc} is a circulant, symmetrical matrix, where every column vector is obtained by rotating one element to the bottom of the preceding column vector.

3.2.3. The Primitive Inductance Tensor of an Eccentric IM

In the case of rotor eccentricity the air gap length is not uniform, because the rotor center O_r does not coincide with the stator center O_s , as shown in Figure 3.

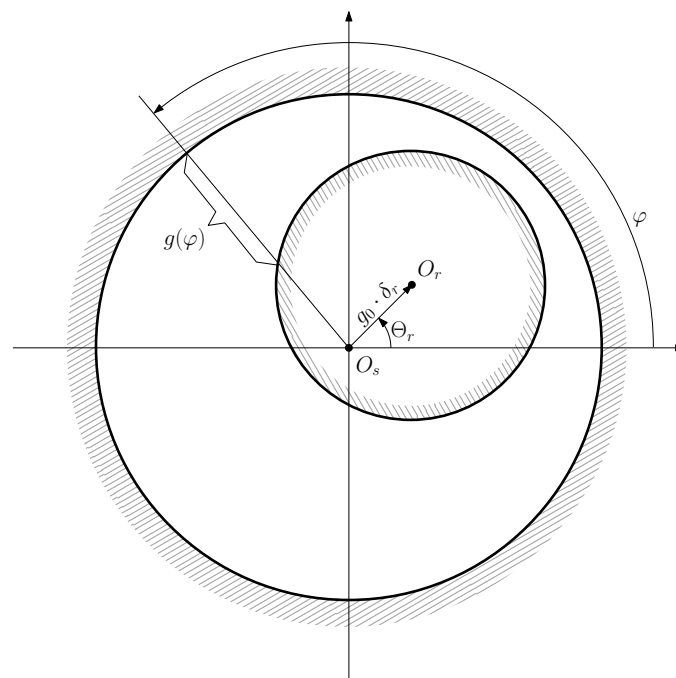


Figure 3. Air gap length $g(\varphi)$ of an eccentric machine as a function of the angular coordinate φ , measured in the canonical coordinate system. The function $g(\varphi)$ is fully defined by the position of the rotor center O_r with respect to the stator center O_s .

From Figure 3, the position of the rotor center can be represented using its radial coordinate, $\delta_r \cdot g_0$, and its angular coordinate Θ_r , as

$$\overrightarrow{O_s O_r} = g_0 \cdot \delta_r \cdot e^{j\Theta_r} \quad 0 \leq \delta_r < 1, 0 \leq \Theta_r < 2\pi \quad (17)$$

where g_0 is the air gap length of the IM without any eccentricity, and δ_r is the degree of eccentricity ($0 \leq \delta_r < 1$). Additionally, the coordinates $(g_0 \cdot \delta_r, \Theta_r)$ of the rotor center depend on the angular position of the rotor θ_r , and the degree of static δ_{se} and dynamic δ_{de} eccentricity of the machine (see Figure 4), as

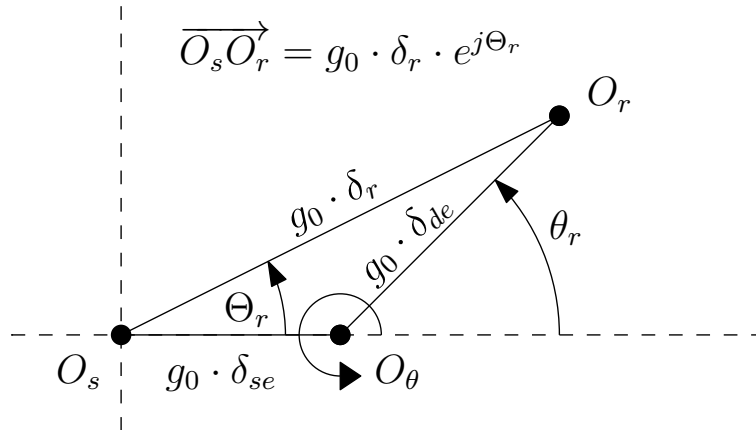


Figure 4. Position of the rotor center (O_r), the stator center (O_s), and the axis of rotation (O_θ) in a coordinate system fixed to the stator, in case of an IM with static (δ_{se}) and dynamic (δ_{de}) eccentricity.

$$\Theta_r(\theta_r) = \tan^{-1} \left(\frac{\delta_{de} \sin(\theta_r)}{\delta_{se} + \delta_{de} \cos(\theta_r)} \right) \quad (18)$$

$$\delta_r(\theta_r) = \sqrt{\delta_{se}^2 + \delta_{de}^2 + 2\delta_{se}\delta_{de} \cos(\theta_r)} \quad (19)$$

where θ_r represents the angle of rotation of the machine rotor.

For computing the inductance matrix, the inverse of the air gap length function is needed to obtain the permeance function of the machine. It can be fully defined in terms of the coordinates of the rotor center (17) as [23]

$$g(\varphi, \Theta_r, \delta_r)^{-1} = g_0^{-1} \cdot \left(A_0 + \sum_{m=1}^{n_t} A_m \cdot \cos(m(\varphi - \Theta_r)) \right) \quad (20)$$

where

$$A_0 = \frac{1}{\sqrt{1 - \delta_r^2}} \quad A_m = 2 \left(\frac{1 - \sqrt{1 - \delta_r^2}}{\sqrt{1 - \delta_r^2}} \right)^m \quad m = 1 \dots n_t \quad (21)$$

It is worth mentioning that only the first term of the series in (20) has been used in [50–53], and two terms in [54]. In this paper, (20) can take into account a generic number n_t of terms, where the value of n_t can be chosen to achieve the desired precision.

Each component (i, j) of the induction matrix L_{mcij} in an eccentric IM depends not only on the angular separation between conductors i and j , but also on their absolute position and on the position of the rotor center, whose coordinates $(g_0 \cdot \delta_r, \Theta_r)$ are, in turn, functions of the rotor angular position (18), (19). The analytical expression of L_{mcij} , for a given rotor position $\theta_k = k \cdot \frac{2\pi}{N}$, can be expressed as [24]

$$L_{mc}(i, j) \Big|_k = \frac{\mu_0 l r}{g_0} \cdot \Lambda\left(i \frac{2\pi}{N}, j \frac{2\pi}{N}, \Theta_r\left(k \frac{2\pi}{N}\right), \delta_r\left(k \frac{2\pi}{N}\right)\right) \quad (22)$$

where

$$\Lambda(\alpha, \varphi, \Theta_r, \delta_r) = \frac{A_0}{4\pi} (\varphi - \alpha)^2 + \sum_{m=1}^{n_t} \frac{A_m}{2\pi} \left(\frac{(\varphi - \alpha) \sin(m(\varphi - \Theta_r))}{m} + \frac{\cos(m(\varphi - \Theta_r))}{m^2} \right) - \left(\frac{1}{2} - K(\alpha, \Theta_r, \delta_r) \right) \cdot \left(A_0 (\varphi - \alpha) + \sum_{m=1}^{n_t} A_m \frac{\sin(m(\varphi - \Theta_r))}{m} \right) \quad (23)$$

and

$$K(\alpha, \Theta_r, \delta_r) = \sum_{m=1}^{n_t} \frac{A_m}{2\pi A_0} \frac{\sin(m(\Theta_r - \alpha))}{m} \quad (24)$$

From (22), the components of L_{mc} are the same for every IM with a given degree of static and dynamic eccentricity, except for the scaling factor $\frac{\mu_0 \cdot l \cdot r \cdot \pi}{g_0}$, which depends only on the geometrical dimensions of the machine.

It is worth remarking that the primitive inductance tensor L_{mc} includes the effect of the air gap asymmetry generated by the mixed eccentricity fault, but is independent of the winding configuration, because it has been obtained using the conductor as the basic unit. Therefore, it is valid for any IM, except for a scaling factor. This leads to a great simplification compared with other existing methods, such as the WFA, which rely on winding functions whose definition depends both on the air gap asymmetry and on the configuration of the winding coils.

3.2.4. Transformation of the Inductance Tensor to Natural Coordinates

In the natural coordinate system, for each rotor position, the inductance tensor L_m in (2) can be obtained from the primitive inductance tensor L_{mc} , either considering healthy (16) or eccentric machine (22), and from the winding tensor C_c , as (5)

$$L_m = C_c^t L_{mc} C_c \quad (25)$$

Again, at this point it is worth remarking that the transformation from the primitive inductance tensor L_{mc} , which includes only the effect of the air gap asymmetry generated by the mixed eccentricity fault, into the final inductance matrix L_m , taking into account the configuration of the windings, is a routine tensor algebra operation (25) that simply consists in multiplying the primitive inductance tensor by the winding tensor C_c (14) (and its transpose). The winding tensor has been defined without any relation to the air gap asymmetry, simply indicating the number and direction of the winding conductors at each interval of the rotor and stator periphery.

This advantage can be further exploited to introduce the effect of winding related faults in the model through the winding tensor C_c , such as inter-turn short circuits or phase asymmetries. This would allow the analysis of combined eccentricity and winding faults with a small increase in analytical and computational complexity. Due to space constraints, this approach has not been considered in this work, and will be presented in a future one.

4. Additional Current Constraints Imposed by Phase Connections

In (3) the phase currents i are independent variables. Nevertheless, the connections between the phases can make some currents dependent on others. These constraints can be expressed as a connection tensor C_i , which relates the original, independent phase currents i (before considering the interconnections between the phases), with the new ones i' , including the constraints introduced by the phase connections as

$$i = C_i i' \quad (26)$$

As the transformation given by C_i is holonomic, because its components do not depend on the rotor position, (1) remains valid when expressed in terms of the new, reduced quantities i' , e' , L' and R' , giving

$$\begin{cases} e' &= R' i' + L' \frac{di'}{dt} + i' \frac{dL'}{d\theta} \dot{\theta} \\ T &= R_\theta \dot{\theta} + J \frac{d\dot{\theta}}{dt} - \frac{1}{2} i'^t \frac{dL'}{d\theta} i' \end{cases} \quad (27)$$

where $e' = C_i^t e$, $R' = C_i^t R C_i$, and $L' = C_i^t L C_i$.

A particular example of current constraints in squirrel cage IMs are those imposed by the physical configuration of the rotor cage, which are analyzed in the following Section.

Current Constraints in a Squirrel Cage IM

In the analytical model of a squirrel cage IM, the n_s stator phases are considered as independent electrical circuits in (3), without any current constraints. Therefore, the resistance and leakage tensors of the stator winding are square matrices of size $n_s \times n_s$, whose diagonal terms are equal to the stator phase resistances, R_s , and to the phase leakage inductances, $L_{\sigma s}$, respectively. All the terms outside the diagonals are zero. If all the stator phases have the same configuration then

$$R_s = \begin{bmatrix} R_s & & 0 \\ & \ddots & \\ 0 & & R_s \end{bmatrix} \quad (28)$$

$$L_{\sigma s} = \begin{bmatrix} L_{\sigma s} & & 0 \\ & \ddots & \\ 0 & & L_{\sigma s} \end{bmatrix} \quad (29)$$

where R_s and $L_{\sigma s}$ are the resistance and the leakage inductance of a stator phase, respectively.

The electric circuit of the squirrel cage rotor, with n_b bars, can be built using n_b rotor loops (each loop formed by two consecutive rotor bars), plus two additional loops corresponding to the end rings [55,56], as represented in Figure 5. The currents in the loops formed by two consecutive bars (i_{b1} to i_{bn_b}) are coupled to each other and to the stator currents through their mutual inductances. On the contrary, the end ring loop currents (i_{e1} and i_{e2} in Figure 5) do not couple with the stator currents, and couple with the other rotor loop currents only through the end ring leakage inductances and the end ring resistances ($L_{\sigma e}$ and R_e in Figure 5, respectively). Therefore, the resistance and leakage tensors of the squirrel cage rotor (with n_b bars) are square matrices of size $(n_b + 2) \times (n_b + 2)$, due to the presence of the two extra loops formed by the end rings.

The resistance matrix of the rotor cage of Figure 5 is given by

$$R_b = \begin{bmatrix} R_{be} & -R_b & & & & & & & -R_e & -R_e \\ -R_b & R_{be} & -R_b & & & & & & -R_e & -R_e \\ & -R_b & R_{be} & -R_b & & & & & -R_e & -R_e \\ & & \ddots & \ddots & \ddots & & & & \vdots & \vdots \\ & & & \ddots & \ddots & \ddots & & & -R_e & -R_e \\ & & & & -R_b & R_{be} & -R_b & & -R_e & -R_e \\ & & & & & -R_b & R_{be} & -R_b & -R_e & -R_e \\ & & & & & & -R_b & R_{be} & -R_e & -R_e \\ \hline -R_e & -R_e & \dots & -R_e & -R_e & -R_e & -R_e & -R_e & n_b R_e & 0 \\ -R_e & -R_e & \dots & -R_e & -R_e & -R_e & -R_e & -R_e & 0 & n_b R_e \end{bmatrix} \quad (30)$$

with $R_{be} = 2(R_b + R_e)$.

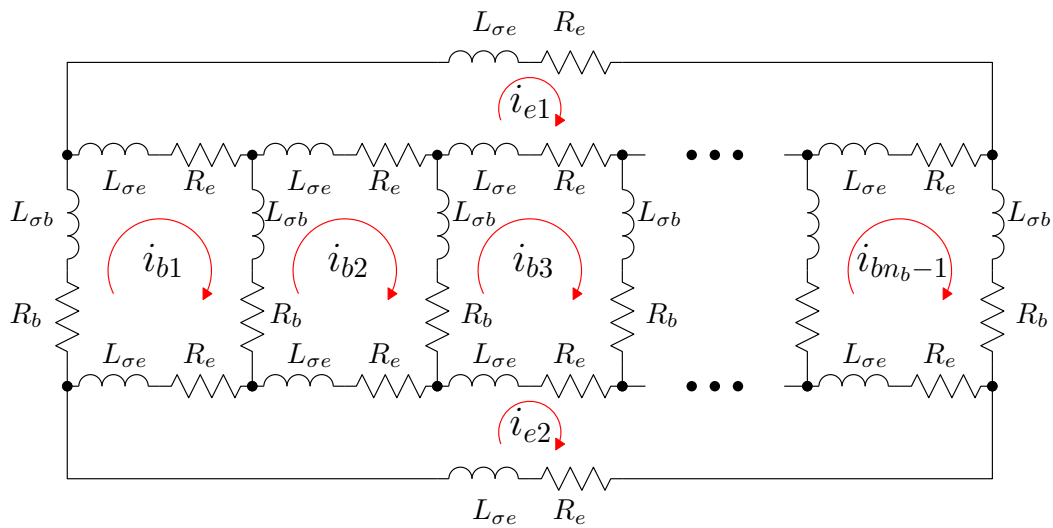


Figure 5. Rotor loops in a squirrel cage rotor of n_b bars. There are $n_b - 1$ rotor loops, formed by two consecutive bars, whose currents (i_{b1} to i_{bn_b-1}) are coupled to each other and to the stator currents through their mutual inductances. Besides, there are two end ring loops, whose currents (i_{e1} and i_{e2}) do not couple with the stator currents, and couple with the other rotor loop currents only through the end ring leakage inductances and the end ring resistances (L_{σ_e} and R_e respectively).

Nevertheless, it is advisable to reduce the set of rotor currents to those circulating in the loops that contain rotor bars, which are the only ones coupled through the mutual loop inductances L_m (25). In this way, the tensor of rotor currents is reduced to

$$i_r = [i_{b1}, i_{b2}, \dots, i_{bn_b-1}]^t \tag{31}$$

This reduction can be achieved because there are two current constraints in the electrical circuit Figure 5. In effect, if the end ring loops mutual inductances with the rest of the rotor loops and with the stator phases are neglected, being mainly end winding flux linkages, the currents in the end ring loops can be expressed as:

$$n_b \left(R_e i_{e1} + L_{\sigma_e} \frac{d i_{e1}}{dt} \right) - \sum_{i=1}^{n_b-1} \left(R_e i_{bi} + L_{\sigma_e} \frac{d i_{bi}}{dt} \right) = 0 \Rightarrow i_{e1} = \frac{1}{n_b} \sum_{i=1}^{n_b-1} i_{bi} \tag{32}$$

$$n_b \left(R_e i_{e2} + L_{\sigma_e} \frac{d i_{e2}}{dt} \right) - \sum_{i=1}^{n_b-1} \left(R_e i_{bi} + L_{\sigma_e} \frac{d i_{bi}}{dt} \right) = 0 \Rightarrow i_{e2} = \frac{1}{n_b} \sum_{i=1}^{n_b-1} i_{bi} \tag{33}$$

These constraints can be formulated as in (26). The old set i_b of $n_b + 1$ rotor currents ($n_b - 1$ current loops that include the bars plus two end ring currents) can be obtained from the new set i_r of $n_b - 1$ currents (just the current loops containing the bars), using (32) and (33), as

$$\underbrace{\begin{bmatrix} i_{b1} \\ i_{b2} \\ \vdots \\ i_{bn_b-1} \\ i_{e1} \\ i_{e2} \end{bmatrix}}_{i_b} \underset{(n_b + 1) \times 1}{=} \underbrace{\begin{bmatrix} 1 & & & & & & \\ & 1 & 0 & & & & \\ & & \ddots & & & & \\ & & & 0 & \ddots & & \\ & & & & & 1 & \\ \hline & \frac{1}{n_b} & \frac{1}{n_b} & \dots & \frac{1}{n_b} & & \\ & \frac{1}{n_b} & \frac{1}{n_b} & \dots & \frac{1}{n_b} & & \end{bmatrix}}_{C_i} \underset{(n_b + 1) \times (n_b - 1)}{\cdot} \underbrace{\begin{bmatrix} i_{b1} \\ i_{b2} \\ \vdots \\ i_{bn_b-1} \end{bmatrix}}_{i_r} \underset{(n_b - 1) \times 1}{\cdot} \tag{34}$$

Using the circuit transformation tensor C_i in (34), which transforms branch resistances into loop ones, as in [57,58], the resistance matrix of the rotor R_r that includes the current constraints (32) and (33) is

$$R_r = C_i^t \cdot R_b \cdot C_i \tag{35}$$

giving the final result

$$R_r = \begin{bmatrix} R_{be} & -R_b & & & & & & & \\ -R_b & R_{be} & -R_b & & & & & & \\ & -R_b & R_{be} & -R_b & & & & & \\ & & \ddots & \ddots & \ddots & & & & \\ \mathbf{0} & & & -R_b & R_{be} & -R_b & & & \\ & & & -R_b & R_{be} & -R_b & & & \\ & & & & -R_b & R_{be} & -R_b & & \\ & & & & & -R_b & R_{be} & & \end{bmatrix} - \frac{2R_e}{n_b} \cdot \begin{bmatrix} 1 & 1 & \dots & 1 \\ 1 & 1 & \dots & 1 \\ \vdots & \vdots & \ddots & \vdots \\ 1 & 1 & \dots & 1 \end{bmatrix} \tag{36}$$

The term $\frac{2R_e}{n_b}$ is small for a high value of n_b , which may justify considering only one end ring current loop, as in [59], or even to neglect both end ring current loops.

In a similar way, the matrix of rotor leakage inductances is given by

$$L_{\sigma r} = \begin{bmatrix} L_{\sigma be} & -L_{\sigma b} & & & & & & & \\ -L_{\sigma b} & L_{\sigma be} & -L_{\sigma b} & & & & & & \\ & -L_{\sigma b} & L_{\sigma be} & -L_{\sigma b} & & & & & \\ & & \ddots & \ddots & \ddots & & & & \\ \mathbf{0} & & & -L_{\sigma b} & L_{\sigma be} & -L_{\sigma b} & & & \\ & & & -L_{\sigma b} & L_{\sigma be} & -L_{\sigma b} & & & \\ & & & & -L_{\sigma b} & L_{\sigma be} & -L_{\sigma b} & & \\ & & & & & -L_{\sigma b} & L_{\sigma be} & & \end{bmatrix} - \frac{2L_{\sigma e}}{n_b} \cdot \begin{bmatrix} 1 & 1 & \dots & 1 \\ 1 & 1 & \dots & 1 \\ \vdots & \vdots & \ddots & \vdots \\ 1 & 1 & \dots & 1 \end{bmatrix} \tag{37}$$

where $L_{\sigma be} = 2(L_{\sigma b} + L_{\sigma e})$.

Using (28), (29), (36) and (37), the final resistance and leakage inductance matrices that are used in the electromechanical equations of the healthy squirrel cage IM are

$$R = \left[\begin{array}{c|c} R_s & 0 \\ \hline 0 & R_r \end{array} \right] \tag{38}$$

$$L_{\sigma} = \left[\begin{array}{c|c} L_{\sigma s} & 0 \\ \hline 0 & L_{\sigma r} \end{array} \right] \tag{39}$$

5. Analytical Model of the Tested IM

In this Section, the analytical model of the commercial IM whose characteristics are given in Appendix A, which is used for the experimental validation of the proposed approach, is calculated considering two different motor conditions:

- Healthy conditions.
- Faulty conditions, with a mixed eccentricity fault, with 30% of static eccentricity ($\delta_{se} = 0.3$) and 30% of dynamic eccentricity ($\delta_{de} = 0.3$).

For building the analytical model of this motor, first the number N of intervals in which the air gap periphery is divided must be selected. In this work, it has been chosen $N = 3600$, giving an angular resolution of 0.1° .

5.1. Analytical Model of the Tested IM in Healthy Conditions

5.1.1. Primitive Inductance Tensor of the Healthy IM

The primitive inductance tensor (15) has been computed for the healthy motor using (16), and its first column is represented in Figure 6. Each one of the rest of the columns of (15) is equal to the previous one, with its elements rotated by one position. This tensor is independent of the angular position of the rotor.

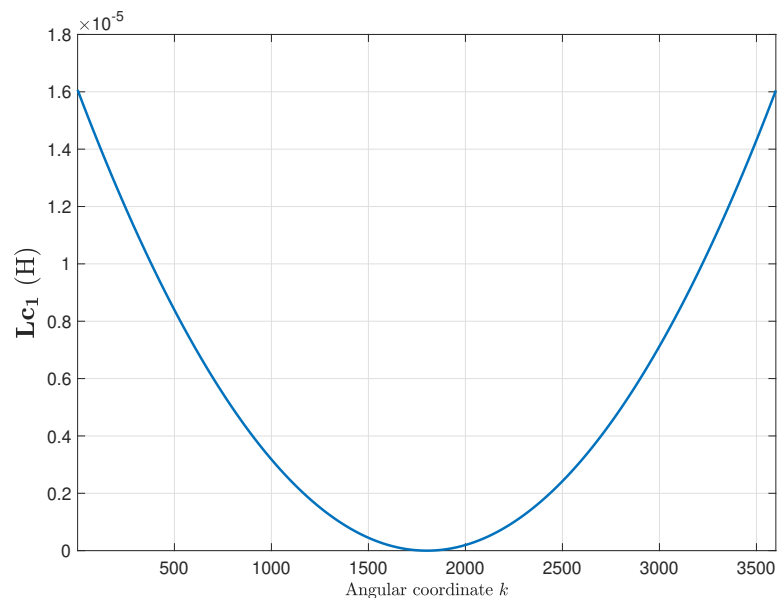


Figure 6. First column of the primitive inductance tensor (15), for the induction machine (IM) given in Appendix A. Each one of the rest of the columns is equal to the previous one, with its element rotated one position.

5.1.2. Winding Tensor of the Healthy IM

The winding tensor, which contains the current-sheet generated by each phase, when fed with a unit current, has been obtained using the data provided in Appendix A. Figure 7 shows the three first columns of the winding tensor C_c (14), corresponding to the stator phases, and Figure 8 shows the next three columns of C_c (14), corresponding to the three first rotor loops. The inclination of rotors slots has been taken into account as in [49].

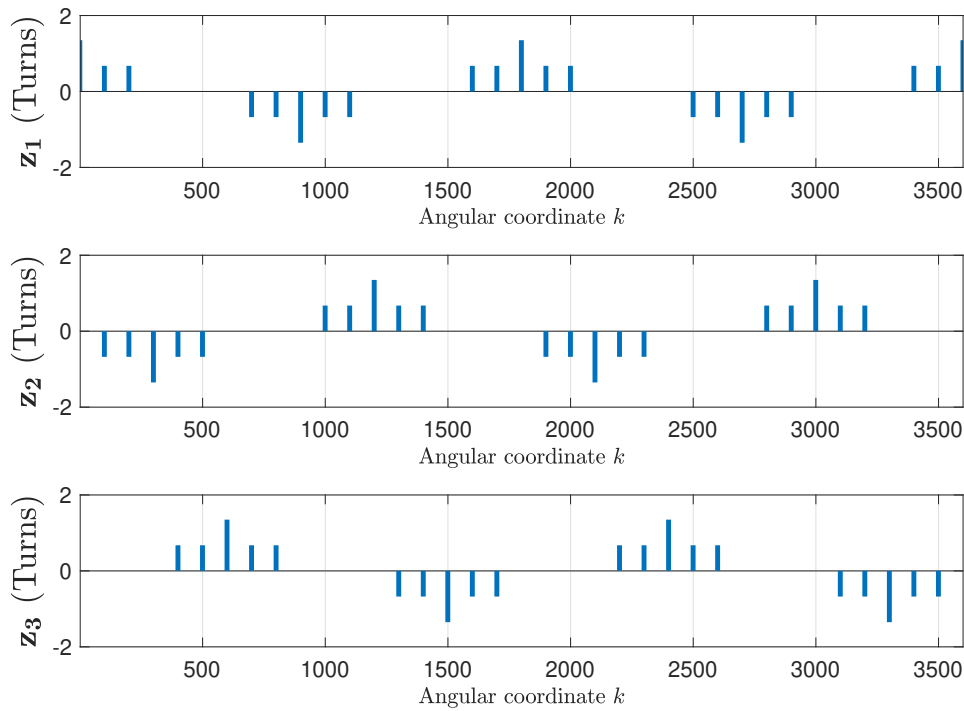


Figure 7. Columns 1–3 of the winding tensor (14), corresponding to the three stator phases of the IM given in Appendix A, which contains the current-sheet generated by each stator phase when fed by a unit current.

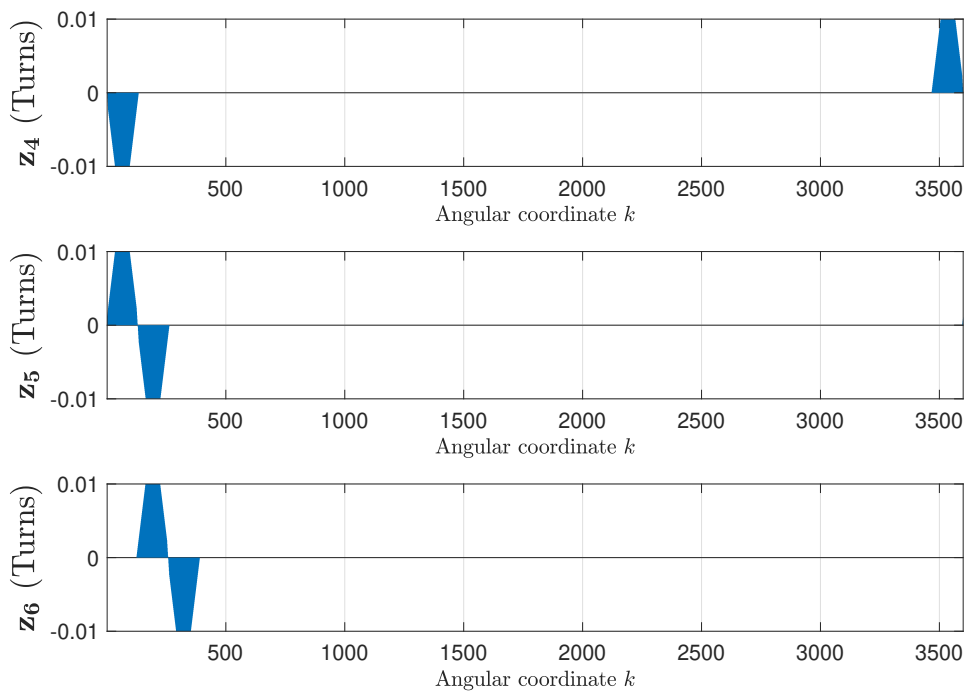


Figure 8. Columns 4–6 of the winding tensor (14), corresponding to the three first rotor loops of the IM given in Appendix A, which contains the current-sheet generated by each rotor loop when fed by a unit current.

5.1.3. Mutual Inductance Matrix of the Healthy IM

The mutual inductance matrix L_m is found applying (15), using the primitive inductance tensor (Figure 9) and the winding tensor (Figures 7 and 8). Figure 9 represents, as a function of the rotor

position, the self-inductance of the first stator phase (Figure 9, top), of the first rotor loop (Figure 9, middle), and the mutual inductance between the first stator phase and the first rotor loop (Figure 9, bottom). Figure 10 shows their respective angular derivatives.

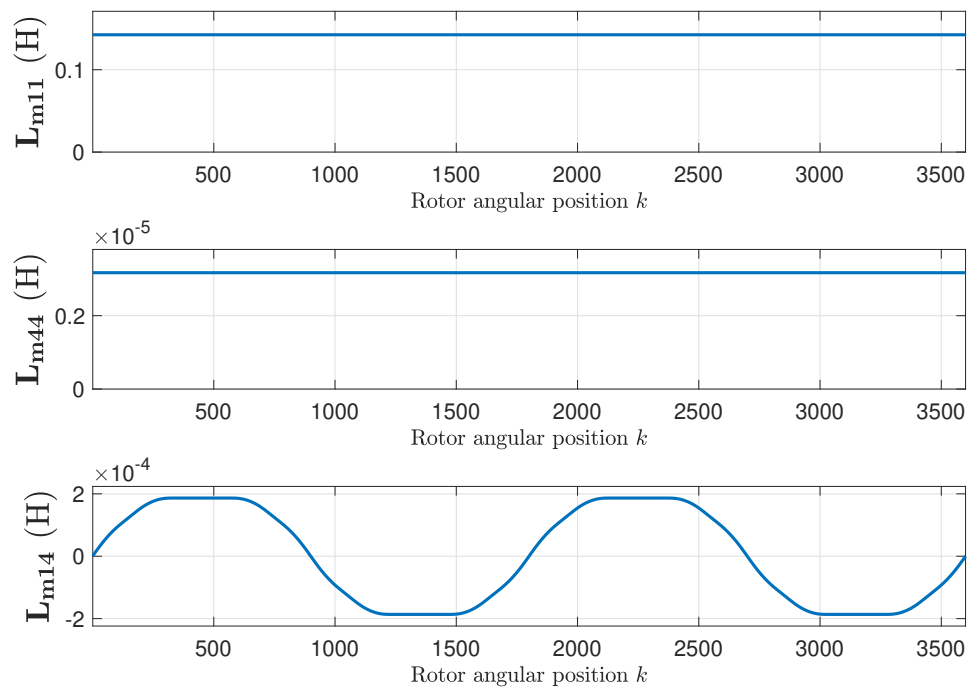


Figure 9. Self-inductance of the first stator phase (**top**), of the first rotor loop (**middle**), and mutual inductance between the first stator phase and the first rotor loop (**bottom**), as a function of the rotor position, for the healthy machine.

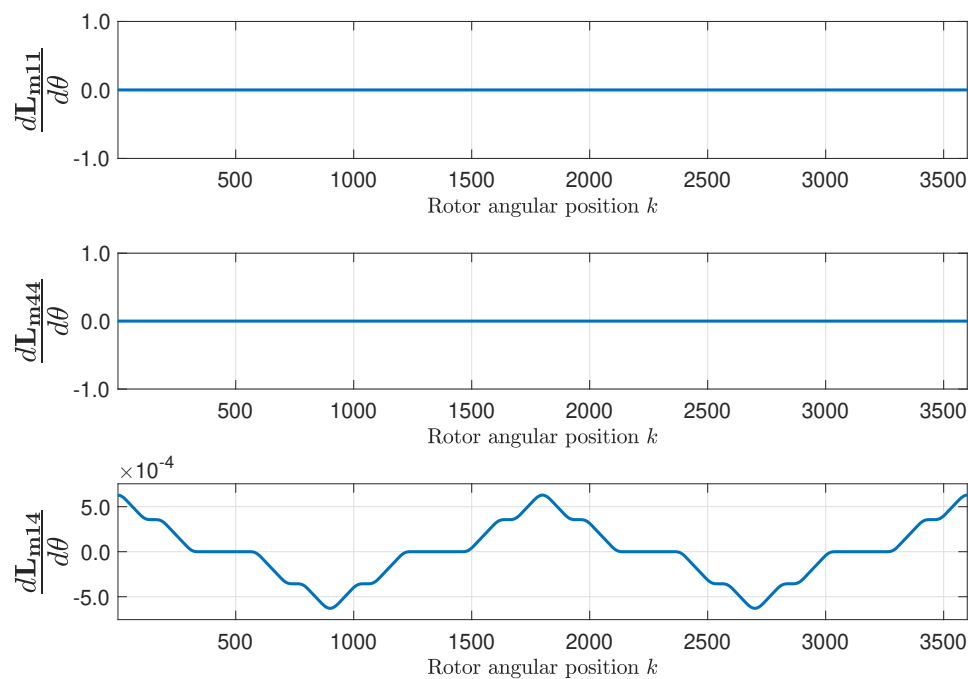


Figure 10. Angular derivatives of the self-inductance of the first stator phase (**top**), of the first rotor loop (**middle**), and mutual inductance between the first stator phase and the first rotor loop (**bottom**), as a function of the rotor position, for the healthy machine.

5.1.4. Resistance and Leakage Inductance Matrices of the Healthy Machine

The resistance (38) and leakage inductance (39) matrices of the healthy machine are assembled using (28), (29), (36) and (37), using the values of the resistance and the leakage inductance of a stator phase, a rotor bar and end ring segment given in Appendix A.

5.2. Analytical Model of the Tested IM with an Eccentricity Fault

The model of the motor given in Appendix A is obtained in this section assuming a mixed eccentricity fault, with a level of 30% of static eccentricity and 30% of dynamic eccentricity ($\delta_{se} = 0.3$, $\delta_{de} = 0.3$). It is modeled using the expression for the primitive inductance tensor of the eccentric IM (22).

5.2.1. Primitive Inductance Tensor of the Eccentric IM

The primitive inductance tensor (15) of the eccentric IM has been computed using (22), using $\delta_{se} = 0.3$ and $\delta_{de} = 0.3$ in (18) and (19). Contrary to the case of the healthy machine, the primitive inductance tensor depends now on the rotor position. The columns of this tensor cannot be obtained by a rotation of the previous ones, due to the eccentricity of the rotor. Figure 11 shows the first column of the primitive inductance tensor, for a rotor angular position equal to zero. It is worth mentioning that the primitive inductance tensor just captures the eccentricity fault, being independent of the winding configuration.

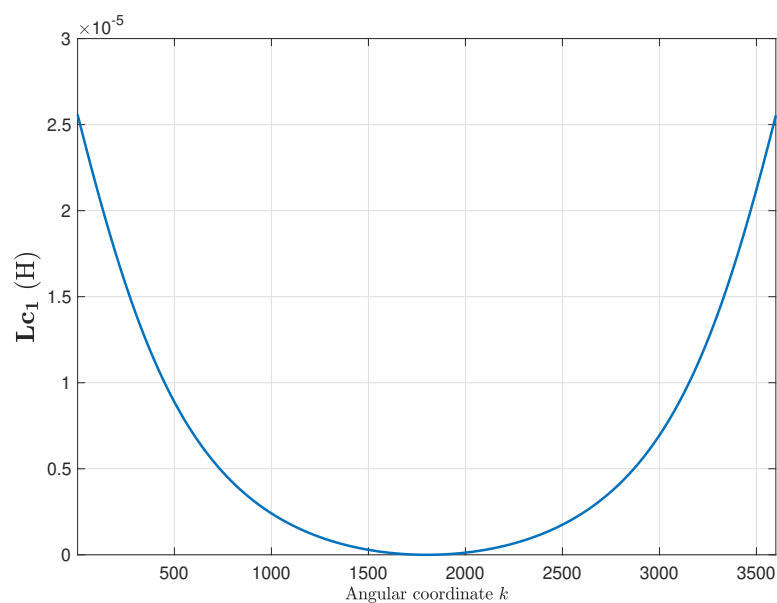


Figure 11. First column of the primitive inductance tensor (15), for the IM given in Appendix A with a mixed eccentricity fault. The other columns of this tensor cannot be obtained by a rotation of this column, due to the eccentricity of the rotor.

5.2.2. Winding Tensor of the Eccentric IM

The winding tensor of the healthy IM, shown in Figures 7 and 8, is not affected by the eccentricity fault. Therefore, it is the same as the winding tensor of the healthy machine.

5.2.3. Mutual Inductance Matrix of the Eccentric IM

The inductance matrix of the faulty IM is found by applying (15), using the primitive inductance tensor represented in Figure 12 and the winding tensor represented in Figures 7 and 8. Figure 12 represents, as a function of the rotor position, the self inductance of the first stator phase (Figure 12, top), of the first rotor loop (Figure 12, middle), and the mutual inductance between the first stator phase and the first rotor loop (Figure 12, bottom). Figure 13 shows their respective angular derivatives.

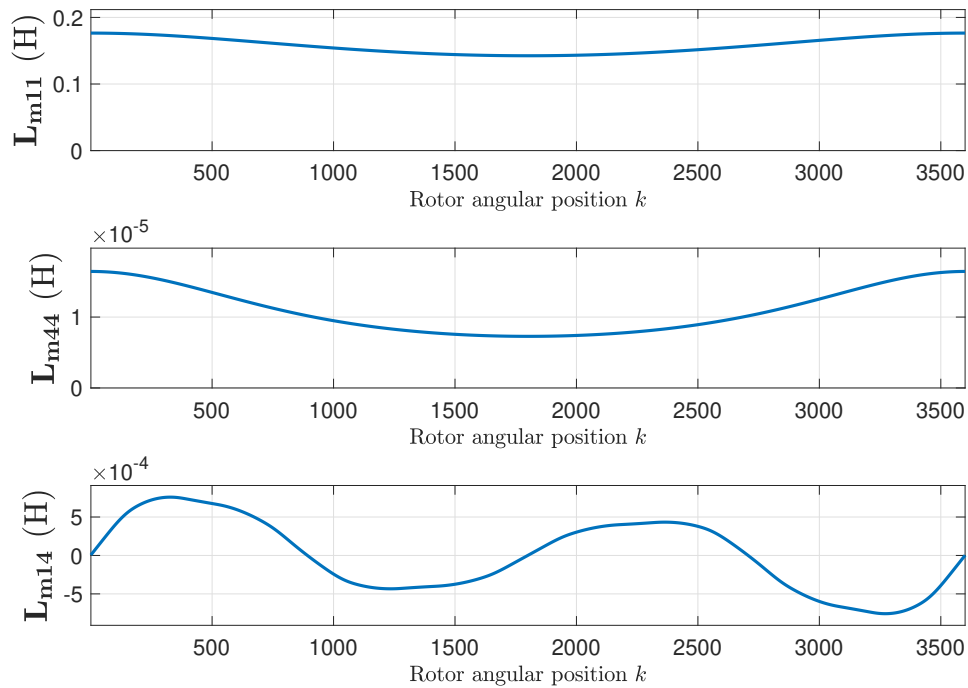


Figure 12. Self-inductance of the first stator phase (**top**), of the first rotor loop (**middle**), and mutual inductance between the first stator phase and the first rotor loop (**bottom**), as a function of the rotor position, for the eccentric machine.

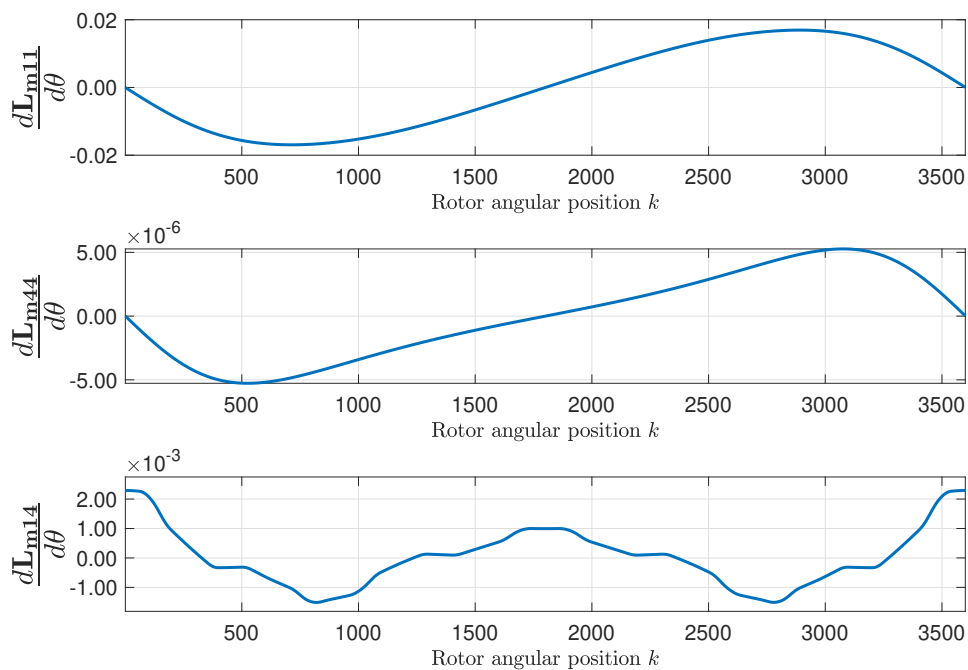


Figure 13. Angular derivatives of the self-inductance of the first stator phase (**top**), of the first rotor loop (**middle**), and mutual inductance between the first stator phase and the first rotor loop (**bottom**), as a function of the rotor position, for the eccentric machine.

5.2.4. Resistance and Leakage Inductance Matrices of the Eccentric Machine

The resistance (38) and leakage inductance (39) matrices of the healthy machine are not affected by the eccentricity fault.

6. Experimental Validation

The experimental procedure carried out for the validation of the proposed method consists in provoking an artificial eccentricity fault to the tested motor (Appendix A), and comparing the characteristic fault harmonics that this fault induces in the motor current with those obtained from the simulated motor. To this end, the original bearings of the motor (see Figure 14a) have been replaced with new bearings (Figure 14d) having a smaller outer diameter and a greater inner diameter. These new bearings have been displaced from the center of the stator bore using two precision eccentric steel rings (Figure 14b,c), placed in the bearings housing (Figure 14b) and on the shaft (Figure 14c). The cylindrical surfaces of both rings are eccentric, 0.09 mm in the case of the outer ring b, and 0.09 mm in the case of the inner ring c. This assembly (Figure 14e) results in a rotor with a 30% of static eccentricity and a 30% of dynamic eccentricity.

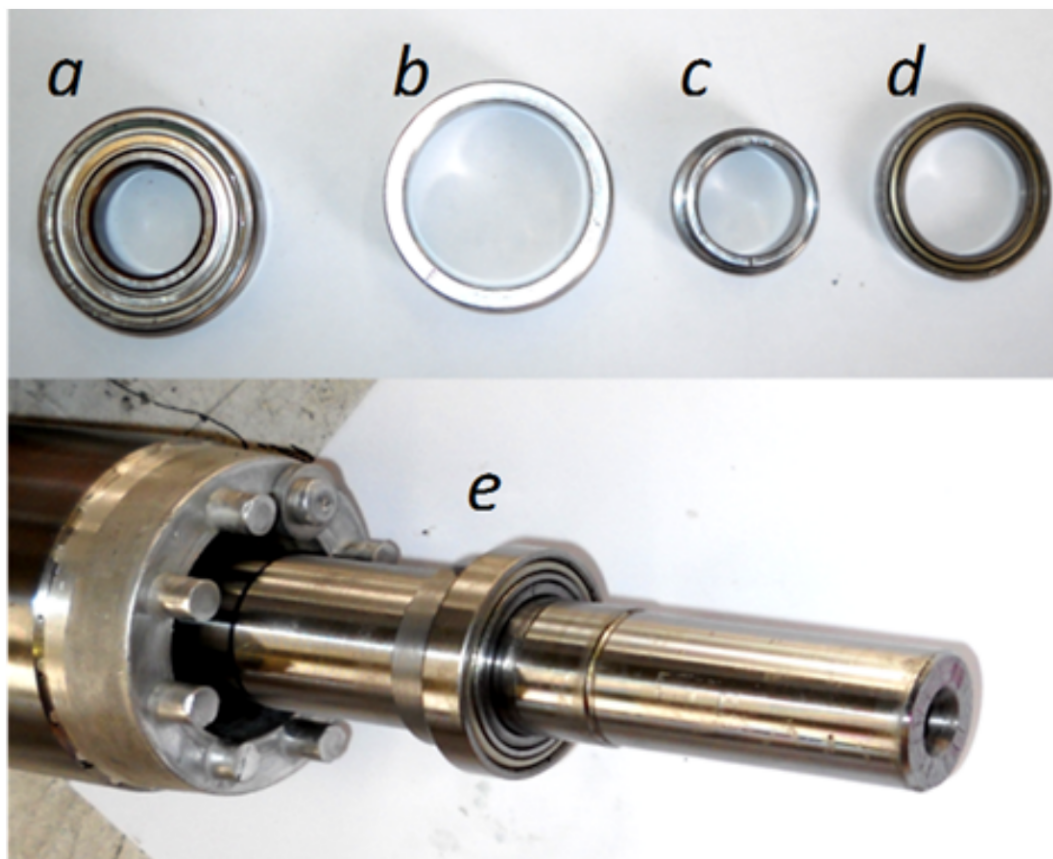


Figure 14. Rotor of the eccentric motor with a provoked mixed eccentricity fault. Top, from left to right: (a) original bearing, (b) external and (c) internal eccentric rings, and (d) new bearing. Bottom: (e) mounted unit on the shaft.

A mixed eccentricity fault [51] induces two characteristic series of harmonic components in the motor current spectrum: one as side bands around the principal slot harmonics, and other one around the fundamental component. The frequencies of this low frequency series depend on the rotor speed, and can be obtained as

$$f_{ME}(s) = f_1 \pm (k(1-s)f_1/p), \quad k = 1, 2, 3 \dots \quad (40)$$

where f_1 is the power supply frequency, s is the slip and p is the number of pole pairs of the machine.

Using the dominant component of the series (40) ($k = 1$), the mixed eccentricity fault can be detected through the presence in the stator current spectrum of harmonic components at frequencies:

$$f_{ME}(s) = f_1 \pm (1-s)f_1/p = f_1 \pm f_r, \quad (41)$$

where f_r is the rotational frequency of the motor. For the tested motor ($p = 2$), this gives

$$f_{ME}(s) = f_1 \pm (1 - s)f_1/2 \quad (42)$$

To verify the validity of the method proposed in this paper, in particular its ability to reproduce the fault harmonics at frequencies given by (42), the eccentric motor has been tested during a start-up transient, with a final permanent regime speed of 1445 rpm ($s = (1500 - 1445)/1500 = 0.0367$). To this end, one of the phase currents has been sampled, using the current clamp whose data is given in Appendix B, during an acquisition time of 8 seconds, with a sampling rate of 2 kHz. The spectrogram of this current, obtained with the computer platform given in Appendix C, is shown in Figure 15. As given by (42), two fault-related harmonics appear in permanent regime at frequencies $f_{ME}(0.0367) = 50 \pm (1 - 0.0367) \cdot 50/2 = [25.92 \text{ Hz}, 74.08 \text{ Hz}]$. Both harmonic components have the same frequency as the fundamental component at the beginning of the start-up transient, and their frequency varies proportionally to the speed up to their final frequency in the permanent regime. For comparison purposes, Figure 16 presents the spectrogram obtained during the start-up transient of the same motor in healthy conditions, prior to provoking the eccentricity fault. In this spectrogram there is no presence of the harmonic components produced by the mixed eccentricity fault.

The motor given in Appendix A has been simulated under the same conditions as the experimental test, using the Simulink model given in Figure 1. The spectrogram of the simulated phase current, shown in Figure 17, displays correctly the characteristic signature of the eccentricity fault harmonics in the time-frequency plane, which assesses the validity of the method presented in this work. For comparison purposes, the motor has been simulated in healthy conditions, and in the spectrogram of its current, shown in Figure 18, there is no presence of the harmonic components produced by the mixed eccentricity fault.

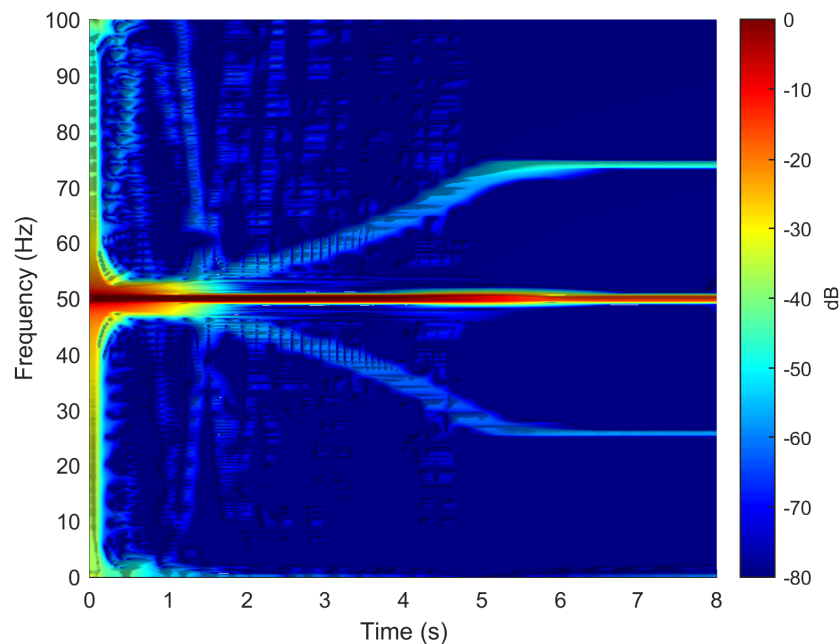


Figure 15. Spectrogram of the experimental current of the motor given in Appendix A, in faulty conditions, obtained during the start up transient. The eccentricity fault related components appear in this time-frequency plot, which indicates a faulty condition.

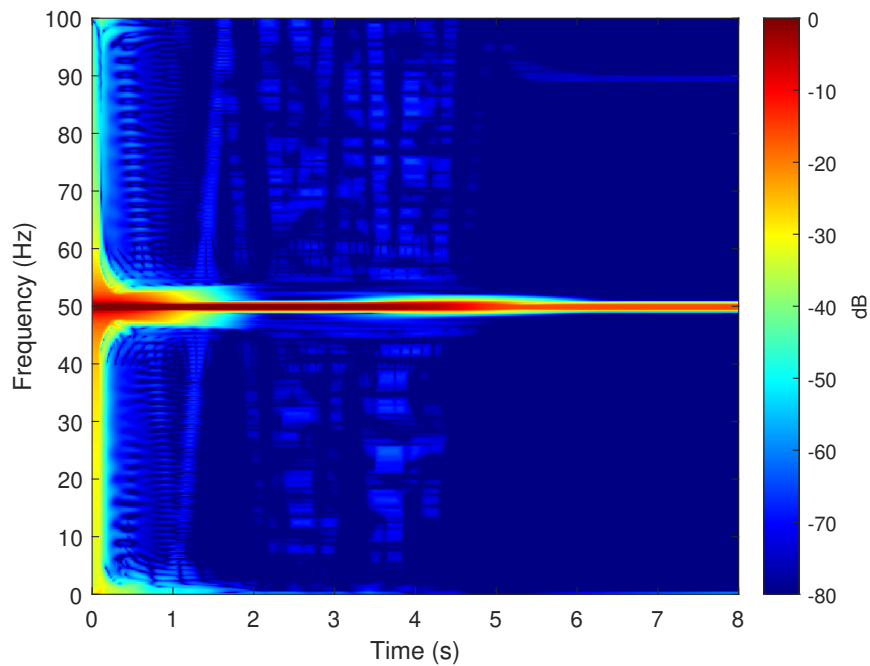


Figure 16. Spectrogram of the experimental current of the motor given in Appendix A, in healthy conditions, obtained during the start up transient. No eccentricity fault related components appear in this time-frequency plot, which indicates a healthy condition.

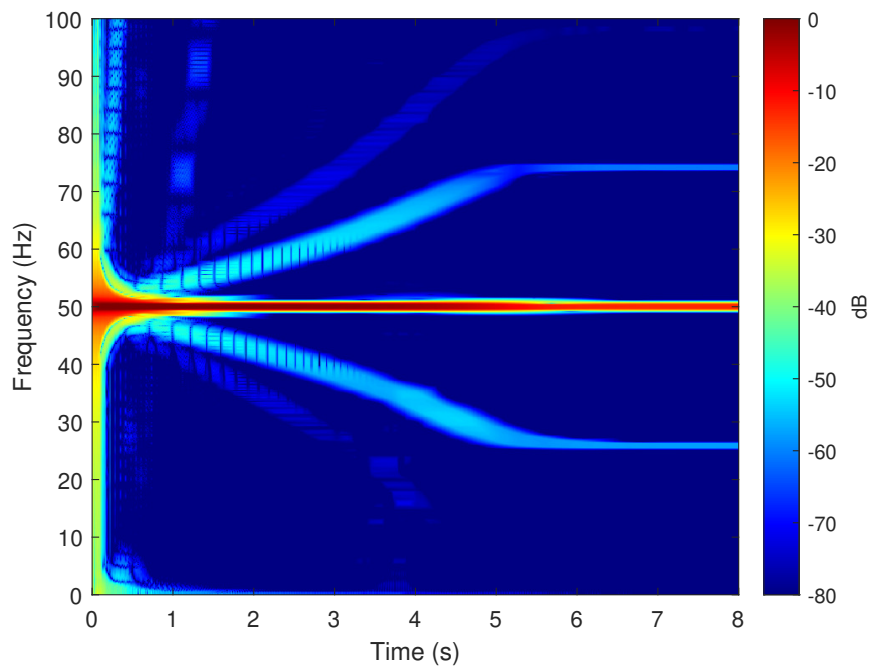


Figure 17. Spectrogram of the simulated current of the motor given in Appendix A, in faulty conditions, obtained during the start up transient. The eccentricity fault related components appear in this time-frequency plot, which indicates a faulty condition.

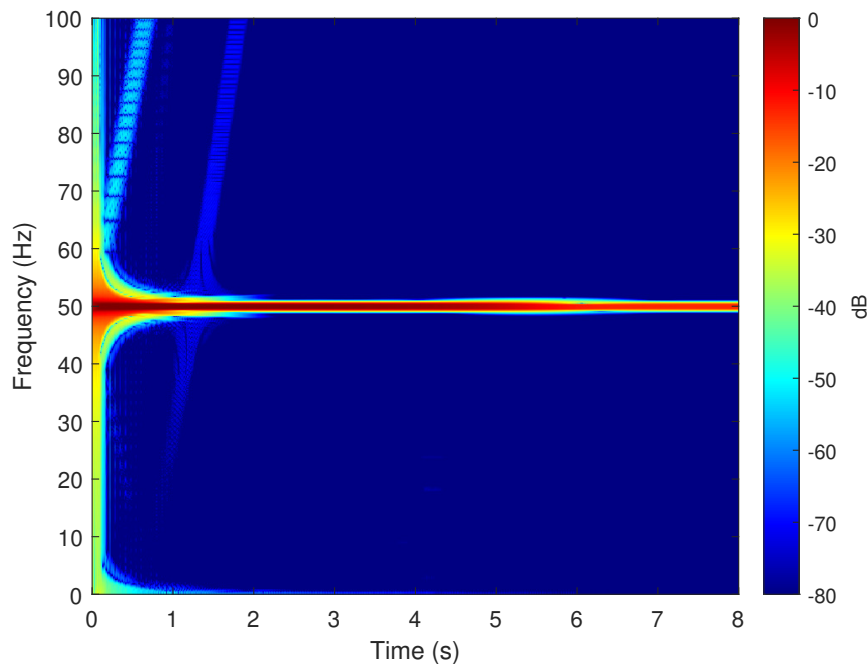


Figure 18. Spectrogram of the simulated current of the motor given in Appendix A, in healthy conditions, obtained during the start-up transient. No eccentricity fault-related components appear in this time-frequency plot, which indicates a healthy condition.

7. Conclusions

Tensor algebra provides a powerful tool for developing the analytical model of IMs, because it allows us to gradually introduce the effects of any fault first at the conductor level, using the primitive inductance tensor, and after at the winding level, using the winding tensor. Routine procedures of tensor algebra facilitate the conversion of the primitive inductance tensor into the inductance matrix of the machine, for any winding configuration. In this work, this new method has been presented, applied to the development of the analytical model of an eccentric IM, and validated using experimental tests. The application of the winding tensor approach for building the analytical model of IMs with other types of faults is currently a work in progress.

Author Contributions: M.P.-S. and M.R.-G. conceived and designed the experiments as well as the conceptualization of the research project; J.P.-C. performed the experiments; R.P.-P. and A.S.-B. analyzed the data; M.P.-S. and J.M.-R. wrote the paper; R.P.-P. was in charge of the project administration. All authors have read and agreed to the published version of the manuscript.

Funding: This research was funded by the Spanish “Ministerio de Ciencia, Innovación y Universidades (MCIU)”, the “Agencia Estatal de Investigación (AEI)” and the “Fondo Europeo de Desarrollo Regional (FEDER)” in the framework of the “Proyectos I+D+i - Retos Investigación 2018”, project reference RTI2018-102175-B-I00 (MCIU/AEI/FEDER, UE).

Conflicts of Interest: The authors declare no conflict of interest.

Appendix A. Commercial IM

Three-phase induction machine. Rated characteristics: $P = 1.1$ kW, $f = 50$ Hz, $U = 400/230$ V, $I = 2.7/4.6$ A, $n = 1410$ r/min, $\cos \varphi = 0.8$.

Machine dimensions: Effective length of the magnetic core = 120 mm, radius at the middle of the air gap = 54.1 mm, air gap length = 0.28 mm.

Stator: Three-phase winding, 36 slots, 78 wires/slot, winding pitch = 7/9, slot opening width = 2.1 mm, phase resistance 7.68 Ω , end winding leakage = 2.3 mH.

Rotor: Squirrel-cage winding, 28 bars, slot opening width = 1.4 mm, skew = one slot pitch, bar resistance = 0.00202 m Ω , end winding leakage = 2.45×10^{-5} mH.

Appendix B. Current Clamp

Chauvin Arnoux MN60, Nominal measuring scope: 100 mA–20A, ratio input/output: 1 A/100 mV, intrinsic error: $\leq 2\% + 50$ mV, frequency use: 40 Hz–10 kHz.

Appendix C. Computer Features

CPU: Intel Core i7-2600K CPU @ 3.40 GHZ RAM memory: 16 GB, Matlab Version: 9.7.0.1216025 (R2019b).

References

- Garramiola, F.; Poza, J.; Madina, P.; del Olmo, J.; Ugalde, G. A Hybrid Sensor Fault Diagnosis for Maintenance in Railway Traction Drives. *Sensors* **2020**, *20*, 962. [[CrossRef](#)] [[PubMed](#)]
- Zamudio-Ramírez, I.; Osornio-Ríos, R.A.; Antonino-Daviu, J.A.; Quijano-Lopez, A. Smart-Sensor for the Automatic Detection of Electromechanical Faults in Induction Motors Based on the Transient Stray Flux Analysis. *Sensors* **2020**, *20*, 1477. [[CrossRef](#)] [[PubMed](#)]
- Casoli, P.; Pastori, M.; Scolari, F.; Rundo, M. A Vibration Signal-Based Method for Fault Identification and Classification in Hydraulic Axial Piston Pumps. *Energies* **2019**, *12*, 953. [[CrossRef](#)]
- Dineva, A.; Mosavi, A.; Gyimesi, M.; Vajda, I.; Nabipour, N.; Rabczuk, T. Fault Diagnosis of Rotating Electrical Machines Using Multi-Label Classification. *Appl. Sci.* **2019**, *9*, 5086. [[CrossRef](#)]
- Zec, F.; Kartalović, N.; Stojić, T. Prediction of high-voltage asynchronous machines stators insulation status applying law on increasing probability. *Int. J. Electr. Power Energy Syst.* **2020**, *116*, 105524. [[CrossRef](#)]
- Elasha, F.; Shanbr, S.; Li, X.; Mba, D. Prognosis of a Wind Turbine Gearbox Bearing Using Supervised Machine Learning. *Sensors* **2019**, *19*, 3092. [[CrossRef](#)] [[PubMed](#)]
- Duong, B.; Khan, S.; Shon, D.; Im, K.; Park, J.; Lim, D.S.; Jang, B.; Kim, J.M. A Reliable Health Indicator for Fault Prognosis of Bearings. *Sensors* **2018**, *18*, 3740. [[CrossRef](#)]
- Qiu, C.; Wu, X.; Xu, C.; Qiu, X.; Xue, Z. An Approximate Estimation Approach of Fault Size for Spalled Ball Bearing in Induction Motor by Tracking Multiple Vibration Frequencies in Current. *Sensors* **2020**, *20*, 1631. [[CrossRef](#)]
- Chen, X.; Feng, Z. Induction motor stator current analysis for planetary gearbox fault diagnosis under time-varying speed conditions. *Mech. Syst. Signal Process.* **2020**, *140*, 106691. [[CrossRef](#)]
- Guellout, O.; Rezig, A.; Touati, S.; Djerdir, A. Elimination of broken rotor bars false indications in induction machines. *Math. Comput. Simul.* **2020**, *167*, 250–266. [[CrossRef](#)]
- Tang, J.; Yang, Y.; Chen, J.; Qiu, R.; Liu, Z. Characteristics Analysis and Measurement of Inverter-Fed Induction Motors for Stator and Rotor Fault Detection. *Energies* **2019**, *13*, 101. [[CrossRef](#)]
- Burriel-Valencia, J.; Puche-Panadero, R.; Martinez-Roman, J.; Sapena-Bano, A.; Pineda-Sanchez, M. Cost-Effective Reduced Envelope of the Stator Current via Synchronous Sampling for the Diagnosis of Rotor Asymmetries in Induction Machines Working at Very Low Slip. *Sensors* **2019**, *19*, 3471. [[CrossRef](#)] [[PubMed](#)]
- Baccarini, L.M.R.; Tavares, J.P.B.; de Menezes, B.R.; Caminhas, W.M. Sliding mode observer for on-line broken rotor bar detection. *Electr. Power Syst. Res.* **2010**, *80*, 1089–1095. [[CrossRef](#)]
- Guezmil, A.; Berriri, H.; Pusca, R.; Sakly, A.; Romary, R.; Mimouni, M.F. Detecting Inter-Turn Short-Circuit Fault in Induction Machine Using High-Order Sliding Mode Observer: Simulation and Experimental Verification. *J. Control. Autom. Electr. Syst.* **2017**, *28*, 532–540. [[CrossRef](#)]
- Yang, H.; Yin, S. Descriptor Observers Design for Markov Jump Systems With Simultaneous Sensor and Actuator Faults. *IEEE Trans. Autom. Control* **2019**, *64*, 3370–3377. [[CrossRef](#)]
- Yang, H.; Yin, S. Reduced-Order Sliding-Mode-Observer-Based Fault Estimation for Markov Jump Systems. *IEEE Trans. Autom. Control* **2019**, *64*, 4733–4740. [[CrossRef](#)]
- Sabouri, M.; Ojaghi, M.; Faiz, J.; Marques Cardoso, A.J. Model-based unified technique for identifying severities of stator inter-turn and rotor broken bar faults in SCIMs. *IET Electr. Power Appl.* **2020**, *14*, 204–211. [[CrossRef](#)]
- Villena-Ruiz, R.; Honrubia-Escribano, A.; Fortmann, J.; Gómez-Lázaro, E. Field validation of a standard Type 3 wind turbine model implemented in DIGSILENT-PowerFactory following IEC 61400-27-1 guidelines. *Int. J. Electr. Power Energy Syst.* **2020**, *116*, 105553. [[CrossRef](#)]

19. Al-Iedani, I.; Gajic, Z. Order reduction of a wind turbine energy system via the methods of system balancing and singular perturbations. *Int. J. Electr. Power Energy Syst.* **2020**, *117*, 105642. [[CrossRef](#)]
20. Lin, Z.; Cevasco, D.; Collu, M. A methodology to develop reduced-order models to support the operation and maintenance of offshore wind turbines. *Appl. Energy* **2020**, *259*, 114228. [[CrossRef](#)]
21. Liang, X.; Ali, M.Z.; Zhang, H. Induction Motors Fault Diagnosis Using Finite Element Method: A Review. *IEEE Trans. Ind. Appl.* **2019**, *56*, 1205–1217. [[CrossRef](#)]
22. Swana, E.F.; Doorsamy, W. Investigation of Combined Electrical Modalities for Fault Diagnosis on a Wound-Rotor Induction Generator. *IEEE Access* **2019**, *7*, 32333–32342. [[CrossRef](#)]
23. Sapena-Bano, A.; Chinesta, F.; Pineda-Sanchez, M.; Aguado, J.; Borzacchiello, D.; Puche-Panadero, R. Induction machine model with finite element accuracy for condition monitoring running in real time using hardware in the loop system. *Int. J. Electr. Power Energy Syst.* **2019**, *111*, 315–324. [[CrossRef](#)]
24. Pineda-Sanchez, M.; Puche-Panadero, R.; Martinez-Roman, J.; Sapena-Bano, A.; Riera-Guasp, M.; Perez-Cruz, J. Partial Inductance Model of Induction Machines for Fault Diagnosis. *Sensors* **2018**, *18*, 2340. [[CrossRef](#)]
25. Sampaio, G.S.; de Aguiar Vallim Filho, A.R.; da Silva, L.S.; da Silva, L.A. Prediction of Motor Failure Time Using An Artificial Neural Network. *Sensors* **2019**, *19*, 4342. [[CrossRef](#)]
26. Yeh, C.H.; Lin, M.H.; Lin, C.H.; Yu, C.E.; Chen, M.J. Machine Learning for Long Cycle Maintenance Prediction of Wind Turbine. *Sensors* **2019**, *19*, 1671. [[CrossRef](#)]
27. Toma, R.N.; Prosvirin, A.E.; Kim, J.M. Bearing Fault Diagnosis of Induction Motors Using a Genetic Algorithm and Machine Learning Classifiers. *Sensors* **2020**, *20*, 1884. [[CrossRef](#)]
28. Burriel-Valencia, J.; Puche-Panadero, R.; Martinez-Roman, J.; Sapena-Bano, A.; Pineda-Sanchez, M.; Perez-Cruz, J.; Riera-Guasp, M. Automatic Fault Diagnostic System for Induction Motors under Transient Regime Optimized with Expert Systems. *Electronics* **2018**, *8*, 6. [[CrossRef](#)]
29. Lei, Y.; Yang, B.; Jiang, X.; Jia, F.; Li, N.; Nandi, A.K. Applications of machine learning to machine fault diagnosis: A review and roadmap. *Mech. Syst. Signal Process.* **2020**, *138*, 106587. [[CrossRef](#)]
30. Wang, X.B.; Zhang, X.; Li, Z.; Wu, J. Ensemble extreme learning machines for compound-fault diagnosis of rotating machinery. *Knowl.-Based Syst.* **2020**, *188*, 105012. [[CrossRef](#)]
31. Rani, M.; Dhok, S.; Deshmukh, R. A Machine Condition Monitoring Framework Using Compressed Signal Processing. *Sensors* **2020**, *20*, 319. [[CrossRef](#)] [[PubMed](#)]
32. Kim, H.; Nerg, J.; Choudhury, T.; Sapanen, J.T. Rotordynamic Simulation Method of Induction Motors Including the Effects of Unbalanced Magnetic Pull. *IEEE Access* **2020**, *8*, 21631–21643. [[CrossRef](#)]
33. Salah, A.A.; Dorrell, D.G.; Guo, Y. A Review of the Monitoring and Damping Unbalanced Magnetic Pull in Induction Machines Due to Rotor Eccentricity. *IEEE Trans. Ind. Appl.* **2019**, *55*, 2569–2580. [[CrossRef](#)]
34. Yassa, N.; Rachek, M.; Houassine, H. Motor Current Signature Analysis for the Air Gap Eccentricity Detection In the Squirrel Cage Induction Machines. *Energy Procedia* **2019**, *162*, 251–262.
35. Rallabandi, V.; Taran, N.; Ionel, D.M.; Zhou, P. Inductance Testing for IPM Synchronous Machines According to the New IEEE Std 1812 and Typical Laboratory Practices. *IEEE Trans. Ind. Appl.* **2019**, *55*, 2649–2659. [[CrossRef](#)]
36. Filipović-Grčić, D.; Filipović-Grčić, B.; Capuder, K. Modeling of three-phase autotransformer for short-circuit studies. *Int. J. Electr. Power Energy Syst.* **2014**, *56*, 228–234.
37. Kim, Y.H.; Lee, J.H. Comparison characteristics of various SynRMs through FEM and experimental verification. *Phys. B Condens. Matter* **2018**, *549*, 69–73. [[CrossRef](#)]
38. Ebadi, F.; Mardaneh, M.; Rahideh, A. Inductance analytical calculations of brushless surface-mounted permanent-magnet machines based on energy method. *COMPEL- Int. J. Comput. Math. Electr. Electron. Eng.* **2019**, *38*, 536–556. [[CrossRef](#)]
39. Fu, Q.; Yue, S.; He, B.; Fu, N. Multiple coupled circuit modelling approach for squirrel cage induction machine under single-broken-bar fault with stator winding functions decomposed in d–q rotor reference frame. *IET Electr. Power Appl.* **2019**, *13*, 889–900.
40. Kron, G.; Hoffmann, B. *Tensor for Circuits*; Dover Books on Science; Dover: New York, NY, USA, 1959.
41. Faiz, J.; Rezaee-Alam, F. A new hybrid analytical model based on winding function theory for analysis of surface mounted permanent magnet motors. *COMPEL- Int. J. Comput. Math. Electr. Electron. Eng.* **2019**, *38*, 745–758.
42. Bewley, L.V. Tensor Algebra in Transformer Circuits. *Trans. Am. Inst. Electr. Eng.* **1936**, *55*, 1214–1219. [[CrossRef](#)]

43. Kron, G. Non-Riemannian Dynamics of Rotating Electrical Machinery. *J. Math. Phys.* **1934**, *13*, 103–194.
44. Ikeda, M.; Hiyama, T. Simulation Studies of the Transients of Squirrel-Cage Induction Motors. *IEEE Trans. Energy Convers.* **2007**, *22*, 233–239.
45. Alberti, L.; Bianchi, N.; Bolognani, S. A Very Rapid Prediction of IM Performance Combining Analytical and Finite-Element Analysis. *IEEE Trans. Ind. Appl.* **2008**, *44*, 1505–1512. [[CrossRef](#)]
46. Jan, S. Determination of slot leakage inductance for three-phase induction motor winding using an analytical method. *Arch. Electr. Eng.* **2013**, *62*, 569–591.
47. Degeneff, R.C.; Gutierrez, M.R.; Salon, S.J.; Burow, D.W.; Nevins, R.J. Kron's reduction method applied to the time stepping finite element analysis of induction machines. *IEEE Trans. Energy Convers.* **1995**, *10*, 669–674. [[CrossRef](#)]
48. Grover, F.W. *Inductance Calculations*; Van Nostrand: New York, NY, USA, 1946.
49. Sapena-Bano, A.; Martinez-Roman, J.; Puche-Panadero, R.; Pineda-Sanchez, M.; Perez-Cruz, J.; Riera-Guasp, M. Induction machine model with space harmonics for fault diagnosis based on the convolution theorem. *Int. J. Electr. Power Energy Syst.* **2018**, *100*, 463–481. [[CrossRef](#)]
50. Joksimovic, G.; Durovic, M.; Penman, J.; Arthur, N. Dynamic simulation of dynamic eccentricity in induction machines-winding function approach. *IEEE Trans. Energy Convers.* **2000**, *15*, 143–148.
51. Nandi, S.; Bharadwaj, R.M.; Toliyat, H.A. Performance Analysis of a Three-Phase Induction Motor Under Mixed Eccentricity Condition. *IEEE Trans. Energy Convers.* **2002**, *17*, 392–399. [[CrossRef](#)]
52. Faiz, J.; Tabatabaei, I. Extension of winding function theory for nonuniform air gap in electric machinery. *IEEE Trans. Magn.* **2002**, *38*, 3654–3657.
53. Bossio, G.; DeAngelo, C.; Solsona, J.; Garcia, G.; Valla, M. A 2-D Model of the Induction Machine: An Extension of the Modified Winding Function Approach. *IEEE Trans. Energy Convers.* **2004**, *19*, 144–150.
54. Faiz, J.; Ardekaneh, I.; Toliyat, H. An Evaluation of Inductances of a Squirrel-Cage Induction Motor under Mixed Eccentric Conditions. *IEEE Trans. Energy Convers.* **2003**, *18*, 252–258.
55. El Malek, M.B.A.; Abdelsalam, A.K.; Hassan, O.E. Novel approach using Hilbert Transform for multiple broken rotor bars fault location detection for three phase induction motor. *ISA Trans.* **2018**, *80*, 439–457. [[CrossRef](#)] [[PubMed](#)]
56. Sudhoff, S.D.; Kuhn, B.T.; Corzine, K.A.; Branecky, B.T. Magnetic Equivalent Circuit Modeling of Induction Motors. *Energy* **2007**, *22*, 259–270. [[CrossRef](#)]
57. Xu, Z.; Ravelo, B.; Maurice, O.; Gantet, J.; Marier, N. Radiated EMC Kron's Model of 3-D Multilayer PCB Aggressed by Broadband Disturbance. *IEEE Trans. Electromagn. Compat.* **2019**, *62*, 406–414. [[CrossRef](#)]
58. Cordier, J.; Kennel, R. A Simple and Efficient State-Space Model of Induction Machines with Interconnected Windings Including Space Harmonics. In Proceedings of the 2018 IEEE Energy Conversion Congress and Exposition (ECCE), Portland, OR, USA, 23–27 September 2018; pp. 1595–1602.
59. Toliyat, H.A.; Lipo, T.A. Transient Analysis of Cage Induction Machines under Stator, Rotor Bar and End Ring Faults. *IEEE Trans. Energy Convers.* **1995**, *10*, 241–247.

